# Mirror-Assisted Calibration of a Multi-modal Sensing Array with a Ground Penetrating Radar and a Camera

Chieh Chou, Shu-Hao Yeh, and Dezhen Song

***Abstract*—To develop a multi-modal in-traffic bridge deck scanning device, we need to estimate the relative pose between a ground penetrating radar (GPR) and a camera. Unlike camera images, GPR output is in a non-Euclidean coordinate system because it only detects underground objects relative to road surface. When road surface is non-planar, its output cannot be trivially mapped to a 3D Cartesian system which is necessary for the sensor fusion. Since there is no joint coverage between two sensors due to mounting requirements, we design an artificial planar bridge assisted by a planar mirror as the calibration rig. We combine the pinhole camera model with mirror reflection transformation and model the GPR imaging process. We estimate the camera and mirror poses and extract readings from hyperbolas generated from metal balls. We employ the maximum likelihood estimator to estimate the rigid body transformation between the two sensors and provide the closed form error analysis. We have conducted physical experiments to validate our calibration process and shown the average error of 6.67 mm for our calibration model. The result is satisfying considering the GPR signal wave length is 18.75 cm.**

***Index Terms*—Calibration, ground penetrating radar, cameras, mirrors.**

## I. Introduction

We are interested in developing automatic scanning devices for in-traffic bridge deck inspection, which requires us to combine a ground penetrating radar (GPR) with a camera to form a multi-sensor suite that is capable of simultaneously performing both subsurface and surface inspection. Fusing the data from different sensors is nontrivial. Unlike the camera, the intrinsic 3D coordinate system of a GPR is not necessarily Euclidean because its horizontal plane is assumed to be overlapped with the road plane. When the road surface is non-planar, its output cannot be directly aligned with Euclidean 3D structure constructed from the camera. Moreover, due to the fact that the field of view (FOV) of the camera is facing forward while the sensing direction of the GPR is downward to the ground, the sensing regions of the two sensors do not overlap, which makes the calibration more challenging. Therefore, before fusing camera and GPR sensory data, we have to design a calibration rig and a scheme to estimate the relative pose (i.e. rotation and translation difference in coordinate systems) between the GPR and the camera in the sensing suite.

Here we propose a calibration process and a method to estimate the relative pose between a GPR and a camera. As illustrated in Fig. 1 top, we design an artificial planar bridge with a planar mirror as the calibration rig to ensure the GPR output coordinate is Euclidean and both sensors can detect the calibration object simultaneously, where a metal ball and a checkerboard have been combined as a combo calibration object. Both GPR data, which is in the form of hyperbolas (see Fig. 1 bottom right) and camera images (see Fig. 1 bottom left) are synchronized by the mechanical stops and guard rails on the calibration rig. To process the calibration data, we first estimate camera and mirror poses using checkerboards which provide an initial solution for camera extrinsic parameters. Second, we perform extrinsic calibration for the GPR to obtain its initial pose. The initial solutions from both sensors are then fed into a Maximum Likelihood Estimator (MLE) for refinement. We formulate this MLE problem and provide the closed form analysis for the error distribution of calibration results. We have tested our calibration method in physical experiments and results show that the calibrated model has an average error of 6.67 mm for testing samples. Considering the GPR signal wave length is 18.75 cm, the results are satisfying.

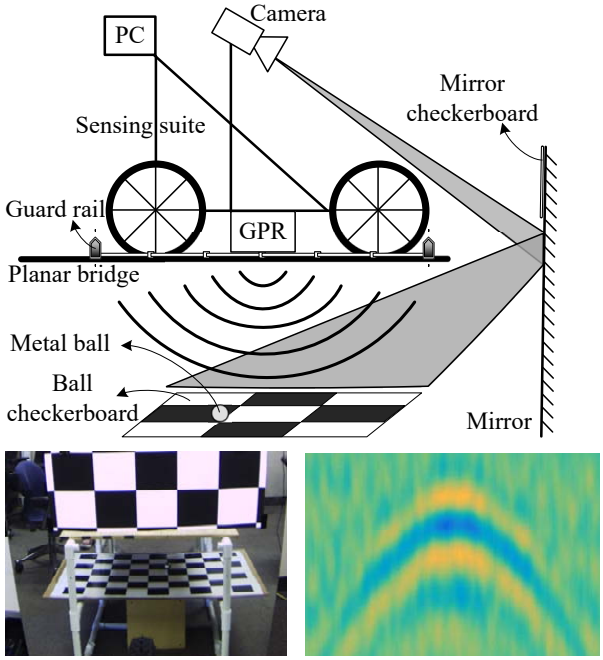


Fig. 1. Top: The artificial planar bridge with a planar mirror is served as the calibration platform for the camera and the GPR. Bottom left: The camera image shows the mirror checkerboard attached on the mirror and the ball checkerboard reflected by the mirror. Bottom right: The GPR image shows a hyperbola response which is generated by GPR sensing the metal ball.

## II. Related Work

Calibration is an important technique to improve the accuracy of a mechanism or a sensor. It usually contains three main components: a model, measurements, and a parameter estimation process [1]. It begins with a closed-form geometry and/or physical model that characterizes a mechanism or a sensing phenomenon. A calibration process is to collect measurements

C. Chou, S. Yeh, and D. Song are with CSE Department, Texas A&M University, College Station, TX 77843, USA, Email: dzsong@cs.tamu.edu.

This work was supported in part by National Science Foundation under IIS-1318638, NRI-1426752, and NRI-1526200, and in part by Texas Department of Transportation (TxDot) 0-6869.

to estimate the model parameters. The measurements are always noisy which is often described by statistical error models. The error models can be obtained either analytically or statistically. A Gaussian distribution is a common error model due to its robust asymptotic probability attributes in large populations [2]. The parameter estimation process finds the model parameters by minimizing an aggregated error metric function.

Mechanism calibration often solves the kinematic parameters and the inertial parameters for mechanisms with prismatic or revolute joints. In robotics and automation, mechanism calibration includes robot manipulator calibration [3], pan-tilt robotic cameras calibration [4], and hand-eye calibration [5]. Sensor calibration differs from mechanism calibration due to the unique combination of intrinsic calibration and extrinsic calibration. While the extrinsic model is the similar 6 degrees of freedom (DoFs) rigid body transformation, the intrinsic model describes the underlying physical principles for the sensing [6] process. For example: a camera [7], [8], a radio antenna [9] and a light detection and ranging sensor (LIDAR) [10], [11] are common sensors that need to be calibrated. Moreover, sensor calibration is indispensable for sensor fusion such as the extrinsic calibration of a camera and a 2D LIDAR [12]–[14]. Our problem is to model camera and GPR imaging characteristics and outputs the 6-DoF rigid body transformation to describe their relative pose.

A GPR measures the time between echoes of electromagnetic signals to survey the objects and layers beneath the ground surface and has many important applications [15]–[17]. A GPR can be mounted on a robotic system for mine detection and removal [18]. Also, GPRs can be integrated with other non-destructive techniques for bridge deck inspection and evaluation [19]. Recently, a GPR is carried by a rover combining with additional sensors for planetary exploration [20]. However, the interpretation of a GPR image depends on the geometric relationship between the GPR and its world coordinate system. Thus in order to effectively make use of GPR data or even properly combine GPR data with other sensory data, extrinsic calibration of a GPR is necessary [21].

To calibrate a camera and a GPR is nontrivial due to different sensing modalities and mounting requirements. The camera has to face the object and remain a certain distance away to ensure FOV for surface inspection while a GPR has to be downward facing and close to the ground for subsurface inspection. Because the sensing regions of both sensors do not overlap, we employ a planar mirror to ensure overlapping sensing region in the calibration process. This design is inspired by many existing mirror-assisted camera pose estimation approaches [22]–[29].

In this paper, we focus on estimating the relative position and orientation of the camera and the GPR. Built on our previous work [21] which only focuses on extrinsic calibration of a GPR, we design a new calibration process and propose a dual modal calibration optimization method to solve the relative pose between the camera and the GPR.

## III. System Design and Problem Formulation

Let us begin with introducing the sensing suite and calibration rig designs to facilitate the understanding of this unique calibration problem.

### A. Sensing Suite Design

To inspect bridge deck, we design a sensing suite by combining a camera and a GPR as shown in Fig. 2. The camera is used to scan/inspect surface cracks and the GPR is used to detect subsurface cracks in bridge decks. Due to the coverage requirement, the camera has to be mounted at least 1 meter above the ground. On the other hand, the GPR needs to be placed close to the ground to ensure good radar signal penetration to the concrete bridge deck. To merge the surface scanning results with subsurface data, we need to calibrate the relative pose between the camera coordinate system and the GPR coordinate system. However, the disjoint coverage and the different sensory modality make this calibration process nontrivial.

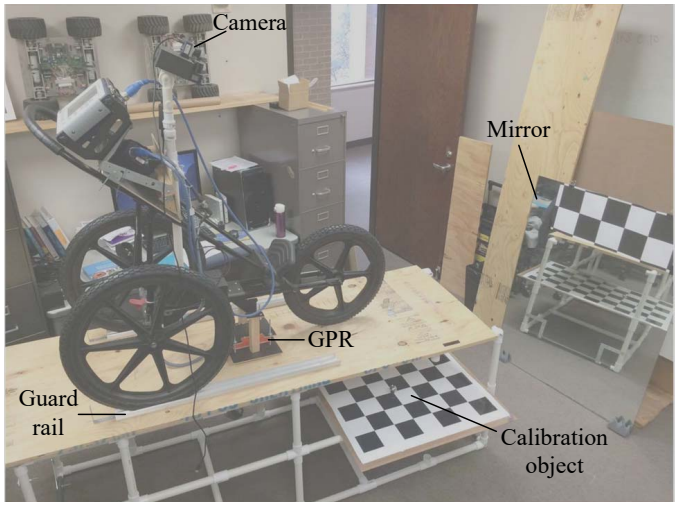


Fig. 2. The sensing suite and the calibration rig design.

### B. Calibration Rig Design

To obtain the relative pose between the GPR and the camera, we design a calibration rig to cope with challenges brought by the two different modalities and their disjoint coverages.

*1) Ensure Euclidean property for the GPR:* The first challenge arises from the fact that a GPR is a terrain following sensor which does not necessarily output sensory data in Euclidean coordinates. If we calibrate the GPR traveling in an arbitrary surface, we cannot obtain proper coordinate system transformation from a non-Euclidean system to the camera coordinate system. To ensure Euclidean sensory data, a GPR must move on a planar surface along a straight linear trajectory. This determines that our calibration rig must be a planar artificial bridge with two guard rails (one for each rear wheel) to ensure that the mounting cart travels in straight line during GPR scanning process (see Fig. 2).

*2) The joint coverage and dual modality signal registration for both sensors:* To obtain the relative pose, it is necessary for the two sensors to detect the collocated calibration objects in the joint coverage space. For the collocated calibration objects, we place a metal ball on top of a wooden checkerboard pattern because the camera and the GPR can detect them respectively. The metal ball is insensitive to orientations and has good reflections to radar signals. The wooden checkerboard pattern can be easily perceived by the camera but not interfere radar signals. Also, we place only one metal ball at one corner of the checkerboard pattern at a time to avoid GPR signal interference. We can adjust the metal ball position for each corner to repeat experiments for more inputs. This "ball-checkerboard" combo is the unique calibration object in our design. We place the combo underneath the artificial bridge where the depth is close to the deck scanning depth. To ensure joint coverage of the two sensors, we install a planar mirror in front of our artificial bridge to create the joint coverage. Also, we attach another checkerboard on the mirror to estimate the mirror pose. Therefore, there are two checkerboards in camera image as shown in Fig. 1 bottom left. We refer to the checkerboard on the mirror as the mirror checkerboard and the checkerboard with the metal ball as the ball checkerboard.

*3) Ensure repeatability and data synchronization:* After placing the metal ball at a corner on the ball checkerboard, we can push the sensing suite to scan the calibration object. A complete scan/trial allows the GPR to generate a hyperbola response in a GPR image (see Fig. 1 bottom right). We adjust the metal ball's position on the ball checkerboard and repeat the process for each metal ball position. We repeat the process for $n$ trials for $n$ positions of the metal ball. The repeatability of each trial is important because we assume GPR follow the same trajectory in the same GPR coordinates. Our guard rails are equipped with $N$ mechanical stops to ensure the repeatability for both sensors to collect data at each stop. This also means that each trial/scan comprises of $N$ data points, each of which includes $N$ camera images and $N$ corresponding points in the GPR image. By taking a camera image and recording the GPR position in the GPR image at each stop (see Fig. 1 bottom left), these $N$ mechanical stops guarantee the data synchronization between the camera and the GPR.

### C. Problem Definition

To focus on the calibrating the relative pose, we assume,

- **a.1** Camera and GPR intrinsic parameters are pre-calibrated.
- **a.2** The measurement noises follow Gaussian distribution with zero means.

Now let us define common notations before introducing the calibration problem.

1) $\{W\}$ and $\{M\}$ denote the 3D world and the mirror coordinate system, respectively. We interchangeably use "frame" and "coordinate system" throughout this paper and let default 3D frames be right-handed coordinates. ${}^{W}\mathbf{B}_i \in \mathbb{R}^3$ denotes the coordinates of $i$-th metal ball center position with respect to $\{W\}$, and ${}^{W}\mathbf{X}_i \in \mathbb{R}^3$ denotes its corresponding point in the checkerboard. As a convention, we will use the left superscript indicates the reference frame in this paper. Without loss of generality, let the checkerboard plane be $Z = 0$ in the world frame, thus we derive ${}^{W}\mathbf{B}_i = {}^{W}\mathbf{X}_i + [0,0,r]^{\mathsf{T}}$, where $r$ is the metal ball radius. ${}^{M}\mathbf{X}_p \in \mathbb{R}^3$ denotes the coordinates of $p$-th point on mirror checkerboard with respect to $\{M\}$.
2) $\{G_k\}$ denotes the GPR frame at stop $k$, where its origin is at the GPR antenna center, its Y-axis is parallel to the GPR moving direction, its Z-axis is perpendicular to the surface plane pointing up, and its X-axis is perpendicular to the GPR moving direction.
3) $\{C_k\}$ denotes the camera frame at stop $k$, where its origin is at the camera optical center, its Z-axis is coinciding with the optical axis and pointing to the forward direction of the camera, and its X-axis and Y-axis are parallel to the horizontal and vertical directions of the CCD sensor plane, respectively.
4) $D_i$ denotes the GPR image which is generated by GPR scanning the $i$-th metal ball. For each $D_i$, we collect $N$ camera images for $N$ mechanical stops, and denote $I_{k,i}$ as the $k$-th camera image.
5) ${}^{G_k}_{C_k}\mathbf{T}$ denotes the rigid body transformation from $\{C_k\}$ to $\{G_k\}$. Since both sensors are fixed firmly on the sensing suite, ${}^{G_1}_{C_1}\mathbf{T}, .., {}^{G_k}_{C_k}\mathbf{T}, ..., {}^{G_N}_{C_N}\mathbf{T}$ are identical. Let ${}^{G}_{C}\mathbf{T} = {}^{G_k}_{C_k}\mathbf{T}$. As a convention, we use left subscript and superscript to indicate frames in the transformation mapping, and left superscript is the final reference frame.

Now we define our calibration problem:

*Definition 1:* Given metal ball coordinates ${}^{W}\mathbf{B}_i$, $i = 1,2,\ldots,n$, where each ${}^{W}\mathbf{B}_i$ has a corresponding GPR image $D_i$ and $N$ camera images $I_{k,i}$, $k = 1,2,\ldots,N$, and mirror checkerboard points ${}^{M}\mathbf{X}_p$ with their corresponding feature points in $I_{k,i}$, determine the rigid body transformation ${}^{G}_{C}\mathbf{T}$.

## IV. Calibration Method

Now let us solve this calibration problem. The computation flow diagram (see Fig. 3) summarizes three main steps: 1) camera and mirror pose estimation, 2) GPR calibration, and 3) dual modal calibration optimization. The first two steps provide initial solutions for the third step. And we also provide error analysis for our calibration results.

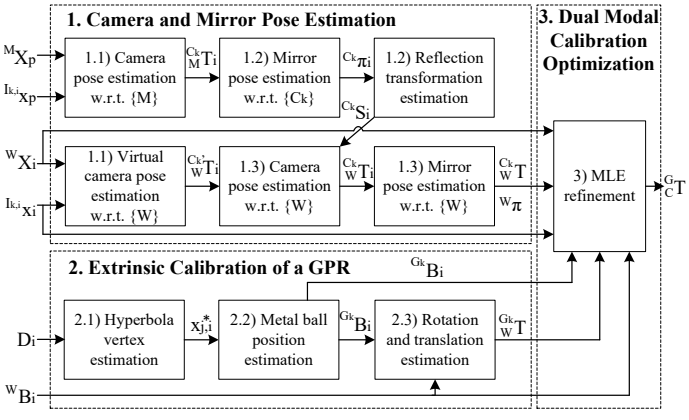


Fig. 3. Calibration computation flow diagram.

### A. Camera and Mirror Pose Estimation

As shown in Fig. 3, we want to find the closed-form solution for the frame mapping from world frame to each camera frame ${}^{C_k}_{W}\mathbf{T}$ and mirror plane in the world frame ${}^{W}\pi$.

*1) Camera pose estimation from 2D/3D points:* Before estimating camera pose, we introduce the camera model. For the mirror checkerboard point ${}^{M}\mathbf{X}_p$, the corresponding 2D image point ${}^{I_{k,i}}\mathbf{x}_p$ in $I_{k,i}$ can be described by the camera projection model [30] as

$$\begin{bmatrix} {}^{I_{k,i}}\mathbf{x}_p \\ 1 \end{bmatrix} = \lambda \mathbf{K} \begin{bmatrix} \mathbf{I}_3 & \mathbf{0}_{3\times 1} \end{bmatrix} {}^{C_k}_{M}\mathbf{T} \begin{bmatrix} {}^{M}\mathbf{X}_p \\ 1 \end{bmatrix}, \tag{1}$$

where $\lambda$ is a scalar, $\mathbf{K}$ is the camera calibration matrix and ${}^{C_k}_{M}\mathbf{T}$ is the rigid body transformation from $\{M\}$ to $\{C_k\}$.

Similarly, for the ball checkerboard point ${}^{W}\mathbf{X}_i$, the corresponding 2D image point ${}^{I_{k,i}}\mathbf{x}_i$ in $I_{k,i}$ through the planar mirror can be described by the camera projection model as

$$\begin{bmatrix} {}^{I_{k,i}}\mathbf{x}_i \\ 1 \end{bmatrix} = \lambda \mathbf{K} \begin{bmatrix} \mathbf{I}_3 & \mathbf{0}_{3\times 1} \end{bmatrix} {}^{C'_k}_{W}\mathbf{T} \begin{bmatrix} {}^{W}\mathbf{X}_i \\ 1 \end{bmatrix}, \tag{2}$$

where ${}^{C'_k}_{W}\mathbf{T}$ represents the mapping from $\{W\}$ to virtual camera frame $\{C'_k\}$ and the apostrophe $'$ indicates the virtual frame in the mirror. It is worth noting that the frames are right-handed coordinates in the real world, but are left-handed in the mirrored space.

Based on the camera model and the 2D/3D corresponding points, we can estimate the rigid body transformation between the reference frame and the camera frame by solving the perspective-n-point (PnP) problem [31], [32]. Therefore, given ${}^{M}\mathbf{X}_p$ and ${}^{I_{k,i}}\mathbf{x}_p$, we can estimate ${}^{C_k}_{M}\mathbf{T}$; given ${}^{W}\mathbf{X}_i$ and ${}^{I_{k,i}}\mathbf{x}_i$, we can estimate ${}^{C'_k}_{W}\mathbf{T}$ .

*2) Mirror pose and reflection transformation estimation w.r.t. $\{C_k\}$:* Let ${}^{C_k}\pi = [{}^{C_k}\mathbf{n}^\mathsf{T}, {}^{C_k}c]^\mathsf{T}$ be the parameters for the planar mirror in $\{C_k\}$, where ${}^{C_k}\mathbf{n}$ is the normal vector of the mirror surface and ${}^{C_k}c$ is the orthogonal distance from the camera origin to the mirror surface. Similarly, ${}^{W}\pi = [{}^{W}\mathbf{n}^\mathsf{T}, {}^{W}c]^\mathsf{T}$ represents the planar mirror in $\{W\}$.

After receiving ${}^{C_k}_{M}\mathbf{T}$ from IV-A1, the mirror parameters ${}^{C_k}\pi$ can be obtained by the plane equation

$${}^{C_k}\mathbf{n}^\mathsf{T}\, {}^{C_k}\mathbf{X} = {}^{C_k}c, \tag{3}$$

where ${}^{C_k}\mathbf{X}$ denotes any point on the mirror plane. Let ${}^{C_k}_{M}\mathbf{T} = \begin{bmatrix} {}^{C_k}_{M}\mathbf{R} & {}^{C_k}_{M}\mathbf{t} \\ \mathbf{0}_{1\times 3} & 1 \end{bmatrix}$ and ${}^{M}\mathbf{X}_p$ be on the plane $Z=0$ in mirror frame $\{M\}$, then ${}^{C_k}\mathbf{n}$ equals to the third column of the rotation matrix ${}^{C_k}_{M}\mathbf{R}$ and ${}^{C_k}c = -{}^{C_k}\mathbf{n}^\mathsf{T}({}^{C_k}_{M}\mathbf{R}^\mathsf{T}\, {}^{C_k}_{M}\mathbf{t})$. Finally, according to the planar mirror model [22]–[27], [29], the mirror reflection transformation in $\{C_k\}$ is obtained by

$${}^{C_k}\mathbf{S} = \begin{bmatrix} \mathbf{I}_3 - 2\,{}^{C_k}\mathbf{n}\,{}^{C_k}\mathbf{n}^\mathsf{T} & 2\,{}^{C_k}c\,{}^{C_k}\mathbf{n} \\ \mathbf{0}_{1\times 3} & 1 \end{bmatrix}. \tag{4}$$

*3) Camera and mirror pose estimation w.r.t. $\{W\}$:* In this section, we want to solve ${}^{C_k}_{W}\mathbf{T}$ and ${}^{W}\pi$. First, we compute ${}^{C_k}_{W}\mathbf{T}$ by using the camera projection model with mirror reflection transformation. Based on ${}^{C'_k}_{W}\mathbf{T}$ in (2) and ${}^{C_k}\mathbf{S}$ in (4), we are able to obtain ${}^{C_k}_{W}\mathbf{T}$ by

$${}^{C_k}_{W}\mathbf{T} = {}^{C_k}\mathbf{S}\, {}^{C'_k}_{W}\mathbf{T}. \tag{5}$$

To increase the accuracy, we average ${}^{C_k}_{W}\mathbf{T}$ over all metal ball center positions $i$, where $i = 1,2,\ldots,n$, as follows.

Let ${}^{C_k}_{W}\mathbf{T} = \begin{bmatrix} {}^{C_k}_{W}\mathbf{R} & {}^{C_k}_{W}\mathbf{t} \\ \mathbf{0}_{1\times 3} & 1 \end{bmatrix}$ be the final transformation we want to estimate and let ${}^{C_k}_{W}\mathbf{T}_i = \begin{bmatrix} {}^{C_k}_{W}\mathbf{R}_i & {}^{C_k}_{W}\mathbf{t}_i \\ \mathbf{0}_{1\times 3} & 1 \end{bmatrix}$ be the measurements with respect to $i$-th metal ball. We use rotation averaging [33] to find the optimal rotation matrix ${}^{C_k}_{W}\mathbf{R}$ by minimizing the following cost function

$$C({}^{C_k}_{W}\mathbf{R}) = \sum_{i=1}^{n} \|{}^{C_k}_{W}\mathbf{R}_i - {}^{C_k}_{W}\mathbf{R}\|_F^2 = C_1 - 2\Big\langle \sum_{i=1}^{n} {}^{C_k}_{W}\mathbf{R}_i, {}^{C_k}_{W}\mathbf{R} \Big\rangle, \tag{6}$$

where $\|\cdot\|_F$ is the Frobenius matrix norm, $\langle\cdot,\cdot\rangle$ is the Frobenius inner product, and $C_1$ is a constant. Thus to minimize (6) becomes

$$\max_{{}^{C_k}_{W}\mathbf{R}\in SO(3)} \Big\langle \sum_{i=1}^{n} {}^{C_k}_{W}\mathbf{R}_i, {}^{C_k}_{W}\mathbf{R} \Big\rangle = \min_{{}^{C_k}_{W}\mathbf{R}\in SO(3)} \|\sum_{i=1}^{n} {}^{C_k}_{W}\mathbf{R}_i - {}^{C_k}_{W}\mathbf{R}\|_F^2. \tag{7}$$

As a result, the closed-form solution for ${}^{C_k}_{W}\mathbf{R}$ is given by ${}^{C_k}_{W}\mathbf{R} = \mathbf{U}\mathbf{S}\mathbf{V}^\mathsf{T}$, where $\mathbf{U}$ and $\mathbf{V}$ are obtained from singular value decomposition of $\sum_{i=1}^{n} {}^{C_k}_{W}\mathbf{R}_i = \mathbf{U}\Sigma\mathbf{V}^\mathsf{T}$, and $\mathbf{S} = diag(1,1,-1)$ if $det(\mathbf{U}\mathbf{V}^\mathsf{T}) \geq 0$, otherwise $\mathbf{S} = \mathbf{I}_{3\times 3}$ because ${}^{C_k}_{W}\mathbf{R}$ is an improper rotation ($det({}^{C_k}_{W}\mathbf{R}) = -1$). Also, we estimate the average translation vector by ${}^{C_k}_{W}\mathbf{t} = \sum_{i=1}^{n} {}^{C_k}_{W}\mathbf{t}_i/n$.

Next, we show how to derive ${}^{W}\pi$. Similarly to (4), the mirror reflection transformation in $\{W\}$ is given by

$${}^{W}\mathbf{S} = {}^{C_k}_{W}\mathbf{T}^{-1}\, {}^{C_k}\mathbf{S}\, {}^{C_k}_{W}\mathbf{T} = \begin{bmatrix} \mathbf{I}_3 - 2\,{}^{W}\mathbf{n}\,{}^{W}\mathbf{n}^\mathsf{T} & 2\,{}^{W}c\,{}^{W}\mathbf{n} \\ \mathbf{0}_{1\times 3} & 1 \end{bmatrix}. \tag{8}$$

Once ${}^{W}\mathbf{S}$ is known, ${}^{W}\pi$ can be obtained by decomposing ${}^{W}\mathbf{S}$. Also, to improve the accuracy, we average ${}^{W}\mathbf{S}$ over all metal ball center positions $i$ and all stops $k$, where $i = 1,2,\ldots,n$ and $k = 1,2,\ldots,N$, as follows.

Let ${}^{W}\mathbf{S} = \begin{bmatrix} {}^{W}\mathbf{R} & {}^{W}\mathbf{t} \\ \mathbf{0}_{1\times 3} & 1 \end{bmatrix}$ be the mirror reflection transformation we want to estimate and let ${}^{W}\mathbf{S}_{k,i} = {}^{C_k}_{W}\mathbf{T}_i^{-1}\, {}^{C_k}\mathbf{S}_i\, {}^{C_k}_{W}\mathbf{T}_i = \begin{bmatrix} {}^{W}\mathbf{R}_{k,i} & {}^{W}\mathbf{t}_{k,i} \\ \mathbf{0}_{1\times 3} & 1 \end{bmatrix}$ be the mirror reflection transformation with respect to $i$-th metal ball at stop $k$. We decompose ${}^{W}\mathbf{t}_{k,i}$ into ${}^{W}c_{k,i}$ and ${}^{W}\mathbf{n}_{k,i}$ by ${}^{W}\mathbf{n}_{k,i} = {}^{W}\mathbf{t}_{k,i}/\|{}^{W}\mathbf{t}_{k,i}\|$ and ${}^{W}c_{k,i} = \|{}^{W}\mathbf{t}_{k,i}\|/2$. Finally, we can obtain ${}^{W}\pi = [{}^{W}\mathbf{n}^\mathsf{T}, {}^{W}c]^\mathsf{T}$ by

$${}^{W}\mathbf{n} = \sum_{i=1}^{n}\sum_{k=1}^{N} \frac{{}^{W}\mathbf{n}_{k,i}}{\|\sum_{i=1}^{n}\sum_{k=1}^{N} {}^{W}\mathbf{n}_{k,i}\|}, \quad {}^{W}c = \sum_{i=1}^{n}\sum_{k=1}^{N} \frac{{}^{W}c_{k,i}}{nN}. \tag{9}$$

### B. Extrinsic Calibration of a GPR

Now we focus on GPR calibration. We want to find metal ball center positions ${}^{G_k}\mathbf{B}_i$ and the frame mapping from $\{W\}$ to each GPR frame ${}^{G_k}_{W}\mathbf{T}$.

Let us introduce the GPR imaging process before explaining the calibration process. The GPR antenna contains a transmitter (TX) and a receiver (RX) [34]. When the GPR moves to perform scanning, it collects all the scans along the trajectory to generate a GPR image. Let a GPR image be $D_i = \{D_{j,i} | j = 1,2,\cdots,m\}$, which consists of $m$ scans. In each scan $D_{j,i}$, the GPR senses the echoed pulse from the $i$-th metal

ball and then records two kinds of measurements. The first is GPR's traveled length $l_j$ measured by its wheel encoder, where $l_j$ is a function of GPR positions at first scan and $j$-th scan. The second is the microwave traveling time from TX to the metal ball to RX. Based on assumption that dielectric material is an uniform dielectric and the microwave's velocity is constant, the traveling time can be converted into the traveling distance. Besides, the TX-RX offset is usually a known intrinsic and pre-compensated in GPR images. Therefore, the microwave traveling time allows the GPR to output a half traveling distance $d_{j,i}$, where $d_{j,i}$ is the function of the GPR position and the metal ball center position. We can assemble $l_j$ and $d_{j,i}$ into a vector $\mathbf{x}_{j,i}$ by

$$\mathbf{x}_{j,i} = \begin{bmatrix} l_j \\ d_{j,i} \end{bmatrix} = \begin{bmatrix} \| {}^{G_j}_{G_1}\mathbf{T}\, {}^{G_1}\mathbf{X}_{ORG} - {}^{G_j}\mathbf{X}_{ORG} \| \\ \| {}^{G_j}\mathbf{X}_i - {}^{G_j}\mathbf{X}_{ORG} \| \end{bmatrix}, \tag{10}$$

where ${}^{G_j}\mathbf{X}_{ORG}$ denotes the origin of $\{G_j\}$ and ${}^{G_j}_{G_1}\mathbf{T}$ is the rigid body transformation from $\{G_1\}$ to $\{G_j\}$. ${}^{G_j}_{G_1}\mathbf{T}$ is a pure translation in our system because of the guard rails.

As shown in Figure 4, a GPR image $D_i$ uses $l_j$ as its horizontal axis and $d_{j,i}$ as its vertical axis. As the GPR moves, a hyperbola is generated. Let $\mathbf{H}_i = \{\mathbf{x}_{j,i} | j = 1,2,\ldots,m\}$ denotes all the points on the hyperbola corresponding to $i$-th metal ball and let $\mathbf{x}_{j^*,i} = [l_{j^*}, d_{j^*,i}]^\mathsf{T}$ be the hyperbola vertex. When the GPR is located at ${}^{G_{j^*}}\mathbf{X}_{ORG}$ along the sensing suite moving direction, $d_{j^*,i}$ is the shortest distance from the GPR to $i$-th metal ball. Therefore, if the GPR moves from scan $j$ to scan $j^*$, then we have $d_{j,i}^2 = d_{j^*,i}^2 + (l_j - l_{j^*})^2$, which can be described in a hyperbola form as

$$\tilde{\mathbf{x}}_{j,i}^\mathsf{T} \mathbf{Q}_i \tilde{\mathbf{x}}_{j,i} = 0, \forall \mathbf{x}_{j,i} \in \mathbf{H}_i, \tag{11}$$

where $\tilde{\mathbf{x}}_{j,i} = [\mathbf{x}_{j,i}^\mathsf{T}, 1]^\mathsf{T}$, $\mathbf{Q}_i = \begin{bmatrix} 1 & 0 & -l_{j^*} \\ 0 & -1 & 0 \\ -l_{j^*} & 0 & l_{j^*}^2 + d_{j^*,i}^2 \end{bmatrix}$, and $l_{j^*}$ and $d_{j^*,i}$ are the parameters of the hyperbola equation. For a general conic equation $ax^2 + bxy + cy^2 + dx + ey + f = 0$ with 5 DoFs, the DoFs in our case decreases to two because $b = e = 0$, and $a = -c = 1$. So two parameters $\{l_{j^*}, d_{j^*,i}\}$ are sufficient to define the corresponding hyperbola.

To calibrate the GPR, there are three steps: 1) hyperbola vertex estimation, 2) metal ball center position estimation, and 3) rotation and translation estimation.

*1) Hyperbola vertex estimation:* First we obtain $\mathbf{x}_{j,i}$ by searching the peak for each scan $D_{j,i}$. Next we have to compensate the metal ball radius $r$ when computing $d_{j,i}$ (the reading from GPR image) by denoting $\tilde{d}_{k,i} = d_{k,i} + r$ as the real distance from the GPR to $i$-th metal ball center position. Then we model $\mathbf{x}_{j,i}$'s measurement error as a zero mean Gaussian with covariance matrix $\sigma_{j,i}^2 \mathbf{I}$. Because $r$ is a constant, the noise distribution of $\tilde{d}_{k,i}$ is the same as that of $d_{k,i}$. By stacking all measurements $\mathbf{x}_{j,i}$ together, we estimate the hyperbola vertex $\mathbf{x}_{j^*,i}$ using the overall error function

$$\phi(\mathbf{x}_{j^*,i}) = \begin{bmatrix} \tilde{\mathbf{x}}_{1,i}^\mathsf{T} \mathbf{Q}_i \tilde{\mathbf{x}}_{1,i} \\ \vdots \\ \tilde{\mathbf{x}}_{m,i}^\mathsf{T} \mathbf{Q}_i \tilde{\mathbf{x}}_{m,i} \end{bmatrix}. \tag{12}$$

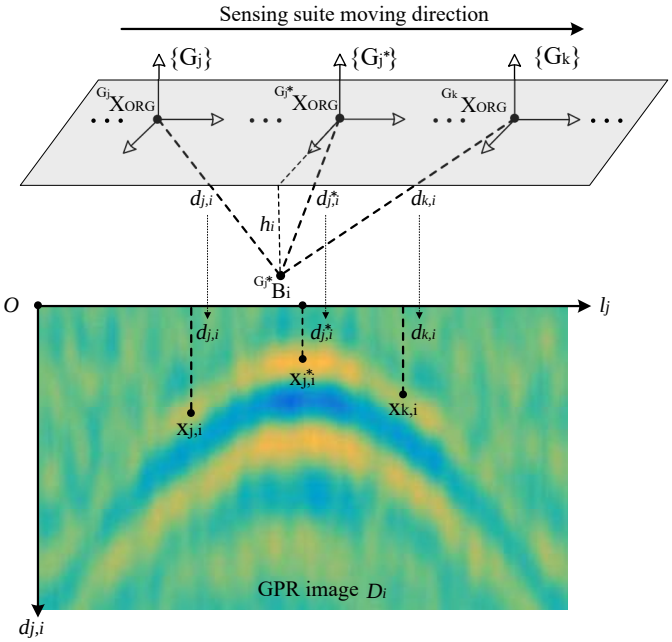


Fig. 4. When the GPR sensing the $i$-the metal ball, it generates a hyperbola response in a GPR image. The index $j$ indicates the $j$-th scan along the trajectory. The index $j^*$ indicates the scan when GPR os closest to the object, which also means the hyperbola vertex. The index $k$ indicates the scan when GPR pauses at mechanical stop $k$.

The MLE of $\mathbf{x}_{j^*,i}$ is obtained by minimizing

$$\min_{\mathbf{x}_{j^*,i}} \phi(\mathbf{x}_{j^*,i})^\mathsf{T} \Sigma_i^{-1} \phi(\mathbf{x}_{j^*,i}), \tag{13}$$

where $\Sigma_i = diag(\sigma_{1,i}^2, \sigma_{2,i}^2, \ldots, \sigma_{m,i}^2)$. This nonlinear optimization problem can be solved by LM algorithm.

*2) Metal ball center position estimation:* Second, let $h_i$ be the vertical distance from $i$-th metal ball center position to the bridge surface, and its noise distribution be zero mean Gaussian with variance $\sigma_{h_i}^2$. Considering the metal ball radius $r$, we use $\tilde{h}_i = h_i - r$ ( $h_i$ is the real measurement from ruler) as the real distance. The noise distribution of $\tilde{h}_i$ is the same as that of $h_i$ because $r$ is a constant. Let $l_k$ be the GPR traveled distance from $\{G_1\}$ to $\{G_k\}$ during the scan. Given $\{\mathbf{x}_{j^*,i}, l_k, \tilde{h}_i\}$, we can compute the metal ball coordinates ${}^{G_k}\mathbf{B}_i$ and its covariance matrix ${}^{G_k}\Sigma_i$ by

$${}^{G_k}\mathbf{B}_i = \begin{bmatrix} \sqrt{\tilde{d}_{j^*,i}^2 - \tilde{h}_i^2} \\ l_{j^*} - l_k \\ -\tilde{h}_i \end{bmatrix}, {}^{G_k}\Sigma_i = J_G \begin{bmatrix} {}^{D_{k,i}}\Sigma & \mathbf{0}_{3\times 1} \\ \mathbf{0}_{1\times 3} & \sigma_{h_i}^2 \end{bmatrix} J_G^\mathsf{T}, \tag{14}$$

where $J_G = \frac{\partial\, {}^{G_k}\mathbf{B}_i}{\partial(\mathbf{x}_{j^*,i}, l_k, \tilde{h}_i)}$ is Jacobian matrix, ${}^{D_{k,i}}\Sigma = \left(J_\phi^T \Sigma_i^{-1} J_\phi\right)^{-1}$ is the covariance matrix of $\{\mathbf{x}_{j^*,i}, l_k\}$, and $J_\phi = \frac{\partial \phi}{\partial(\mathbf{x}_{j^*,i}, l_k)}$ is Jacobian matrix.

*3) Rotation and translation estimation:* Finally, after obtaining the metal ball coordinates of $\{G_k\}$ and $\{W\}$, we can compute the closed-form solution of ${}^{G_k}_{W}\mathbf{T}$ by Horn's method [35] and then refine the solution by MLE. For the error analysis and more details, please refer to [21].

### C. Dual Modal Calibration Optimization

With the initial calibration results from both the camera and the GPR, we can formulate an overall optimization problem to estimate ${}^{G}_{C}\mathbf{T}$, ${}^{W}\pi$, $\{{}^{C_k}_{W}\mathbf{T}|k=1,\ldots,N\}$, $\{{}^{W}\mathbf{X}_i|i=1,\ldots,n\}$, and $\{{}^{W}\mathbf{B}_i|i=1,\ldots,n\}$ based on all the measurements. The relationship of the coordinates systems is given by

$$\begin{bmatrix} {}^{G_k}\mathbf{X}_i \\ 1 \end{bmatrix} = {}^{G_k}_{W}\mathbf{T} \begin{bmatrix} {}^{W}\mathbf{X}_i \\ 1 \end{bmatrix} = {}^{G}_{C}\mathbf{T}\,{}^{C_k}_{W}\mathbf{T} \begin{bmatrix} {}^{W}\mathbf{X}_i \\ 1 \end{bmatrix}. \tag{15}$$

Let ${}^{C_k}_{W}\mathbf{T} = \begin{bmatrix} {}^{C_k}_{W}\mathbf{R} & {}^{C_k}_{W}\mathbf{t} \\ \mathbf{0}_{1\times 3} & 1 \end{bmatrix}$ and let the 6-vector representation of ${}^{C_k}_{W}\mathbf{R}$ and ${}^{C_k}_{W}\mathbf{t}$ be $\xi_k = [\theta_{x,k}, \theta_{y,k}, \theta_{z,k}, t_{x,k}, t_{y,k}, t_{z,k}]^{\mathsf{T}}$, where $(\theta_{x,k}, \theta_{y,k}, \theta_{z,k})$ is the Euler angle representation of ${}^{C_k}_{W}\mathbf{R}$ in the order of Z-Y-X, and ${}^{C_k}_{W}\mathbf{t} = [t_{x,k}, t_{y,k}, t_{z,k}]^{\mathsf{T}}$. The initial value of ${}^{G}_{C}\mathbf{T}$ can be obtained by ${}^{G}_{C}\mathbf{T} = {}^{G_k}_{W}\mathbf{T}\,{}^{C_k}_{W}\mathbf{T}^{-1}$. Let $\eta$ be the 6-vector representation of ${}^{G}_{C}\mathbf{T}$, where the notation definitions are similar to $\xi_k$. Let ${}^{W}\hat{\mathbf{X}}_i$ and ${}^{W}\hat{\mathbf{B}}_i$ be the estimator of ${}^{W}\mathbf{X}_i$ and ${}^{W}\mathbf{B}_i$, respectively. We define the parameterized function for camera as ${}^{I_{k,i}}\mathbf{x}_i = f({}^{W}\pi, \xi_k, {}^{W}\mathbf{X}_i)$ according to (2) and (8), and for GPR as ${}^{G_k}\mathbf{B}_i = g(\eta, \xi_k, {}^{W}\mathbf{B}_i)$ according to (15).

Finally, let $\mathbf{p} = [\eta^{\mathsf{T}}, \xi^{\mathsf{T}}, {}^{W}\pi^{\mathsf{T}}, \mathbf{X}_c^{\mathsf{T}}, \mathbf{X}_g^{\mathsf{T}}]^{\mathsf{T}}$ be the estimated vector, where $\xi = [\xi_1^{\mathsf{T}}, \ldots, \xi_N^{\mathsf{T}}]^{\mathsf{T}}$, $\mathbf{X}_c = [{}^{W}\hat{\mathbf{X}}_1{}^{\mathsf{T}}, \ldots, {}^{W}\hat{\mathbf{X}}_n{}^{\mathsf{T}}]^{\mathsf{T}}$, and $\mathbf{X}_g = [{}^{W}\hat{\mathbf{B}}_1{}^{\mathsf{T}}, \ldots, {}^{W}\hat{\mathbf{B}}_n{}^{\mathsf{T}}]^{\mathsf{T}}$. The cost function is given by

$$\omega(\mathbf{p}) = \begin{bmatrix} \omega_1 \\ \omega_2 \end{bmatrix}, \tag{16}$$

where $\omega_1 = \begin{bmatrix} {}^{W}\hat{\mathbf{X}}_1 - {}^{W}\mathbf{X}_1 \\ \vdots \\ {}^{W}\hat{\mathbf{X}}_n - {}^{W}\mathbf{X}_n \\ \psi_1 \\ \vdots \\ \psi_N \end{bmatrix}$, $\omega_2 = \begin{bmatrix} {}^{W}\hat{\mathbf{B}}_1 - {}^{W}\mathbf{B}_1 \\ \vdots \\ {}^{W}\hat{\mathbf{B}}_n - {}^{W}\mathbf{B}_n \\ \rho_1 \\ \vdots \\ \rho_N \end{bmatrix}$, $\psi_k = \begin{bmatrix} f({}^{W}\pi, \xi_k, {}^{W}\mathbf{X}_1) - {}^{I_k}\bar{\mathbf{x}}_1 \\ \vdots \\ f({}^{W}\pi, \xi_k, {}^{W}\mathbf{X}_n) - {}^{I_k}\bar{\mathbf{x}}_n \end{bmatrix}$ is the camera reprojection error at stop $k$, and $\rho_k = \begin{bmatrix} g(\eta, \xi_k, {}^{W}\hat{\mathbf{B}}_1) - {}^{G_k}\mathbf{B}_1 \\ \vdots \\ g(\eta, \xi_k, {}^{W}\hat{\mathbf{B}}_n) - {}^{G_k}\mathbf{B}_n \end{bmatrix}$ is the metal ball center position estimation error at stop $k$. And ${}^{I_k}\bar{\mathbf{x}}_j$ is denoted by ${}^{I_k}\bar{\mathbf{x}}_j = \frac{\sum_{i=1}^{n} {}^{I_{k,i}}\mathbf{x}_j}{n}$. The MLE of $\mathbf{p}$ is solved by minimizing

$$\min_{\mathbf{p}} \ \omega(\mathbf{p})^{\mathsf{T}} \Sigma_{\omega}^{-1} \omega(\mathbf{p}), \tag{17}$$

where $\Sigma_{\omega} = diag(\Sigma_{\omega_1}, \Sigma_{\omega_2})$, $\Sigma_{\omega_1} = diag({}^{W}\Sigma_1, \ldots, {}^{W}\Sigma_n, \Sigma_{\psi_1}, \ldots, \Sigma_{\psi_N})$, $\Sigma_{\omega_2} = diag({}^{W}\Sigma_1, \ldots, {}^{W}\Sigma_n, \Sigma_{\rho_1}, \ldots, \Sigma_{\rho_N})$, $\Sigma_{\psi_k} = diag({}^{I_k}\Sigma_1, \ldots, {}^{I_k}\Sigma_n)$, $\Sigma_{\rho_k} = diag({}^{G_k}\Sigma_1, \ldots, {}^{G_k}\Sigma_n)$. ${}^{W}\Sigma_i$ and ${}^{I_k}\Sigma_i$ are obtained by direct measurement; ${}^{G_k}\Sigma_i$ is obtained from (14). The problem can be solved by LM algorithm. Lemma 1 shows the covariance of $\eta$ and $\xi$.

*Lemma 1:* Under the Gaussian noise assumption, the covariance matrix of $\eta$ and $\xi$ is given by

$$\Sigma_{\eta,\xi} = (\mathbf{A} - \mathbf{B}\mathbf{D}^{-1}\mathbf{C})^{-1}, \tag{18}$$

where $\mathbf{A}$, $\mathbf{B}$, $\mathbf{C}$, $\mathbf{D}$ are defined in (20).

*Proof:* From the first order approximation of error backward propagation [30], we can obtain the covariance matrix of $\mathbf{p}$ by

$$\Sigma_{\mathbf{p}} = \left(J_{\omega}^{\mathsf{T}} \Sigma_{\omega}^{-1} J_{\omega}\right)^{-1}, \tag{19}$$

where $\Sigma_{\omega}^{-1} = \begin{bmatrix} \Sigma_{\omega_1}^{-1} & \mathbf{0} \\ \mathbf{0} & \Sigma_{\omega_2}^{-1} \end{bmatrix}$ and Jacobian matrices

$$J_{\omega} = \frac{\partial \omega(\mathbf{p})}{\partial \mathbf{p}} = \begin{bmatrix} \mathbf{0} & \mathbf{0} & \mathbf{0} & \mathbf{I} & \mathbf{0} \\ \mathbf{0} & J_{\xi 1} & J_{\pi} & J_{x1} & \mathbf{0} \\ \mathbf{0} & \mathbf{0} & \mathbf{0} & \mathbf{0} & \mathbf{I} \\ J_{\eta} & J_{\xi 2} & \mathbf{0} & \mathbf{0} & J_{x2} \end{bmatrix},$$

$$J_{\eta} = \begin{bmatrix} \frac{\partial \rho_1^{\mathsf{T}}}{\partial \eta}, & \ldots & , \frac{\partial \rho_N^{\mathsf{T}}}{\partial \eta} \end{bmatrix}^{\mathsf{T}}, J_{\pi} = \begin{bmatrix} \frac{\partial \psi_1^{\mathsf{T}}}{\partial {}^{W}\pi}, & \ldots & , \frac{\partial \psi_N^{\mathsf{T}}}{\partial {}^{W}\pi} \end{bmatrix}^{\mathsf{T}},$$

$$J_{\xi 1} = diag\left(\frac{\partial \psi_1}{\partial \xi_1}, \ldots, \frac{\partial \psi_N}{\partial \xi_N}\right), J_{\xi 2} = diag\left(\frac{\partial \rho_1}{\partial \xi_1}, \ldots, \frac{\partial \rho_N}{\partial \xi_N}\right),$$

$$J_{x1} = \begin{bmatrix} \frac{\partial \psi_1^{\mathsf{T}}}{\partial \mathbf{X}_c}, & \ldots & , \frac{\partial \psi_N^{\mathsf{T}}}{\partial \mathbf{X}_c} \end{bmatrix}^{\mathsf{T}}, J_{x2} = \begin{bmatrix} \frac{\partial \rho_1^{\mathsf{T}}}{\partial \mathbf{X}_g}, & \ldots & , \frac{\partial \rho_N^{\mathsf{T}}}{\partial \mathbf{X}_g} \end{bmatrix}^{\mathsf{T}}.$$

To simplify the notations, we denote $\Sigma_{\omega_1}^{-1} = \begin{bmatrix} {}^{C}\Sigma & \mathbf{0} \\ \mathbf{0} & {}^{\psi}\Sigma \end{bmatrix}$, and $\Sigma_{\omega_2}^{-1} = \begin{bmatrix} {}^{G}\Sigma & \mathbf{0} \\ \mathbf{0} & {}^{\rho}\Sigma \end{bmatrix}$, and derive (20) in next page top.

Finally, we can solve $\Sigma_{\eta,\xi}$ through $\Sigma_{\mathbf{p}}$ by applying the block-wise matrix inversion to (20). ■

### D. Rigid Body Transformation Model Error

To verify the results, we use the Euclidean distance between ${}^{G_k}\hat{\mathbf{B}}_i$ and ${}^{G_k}\mathbf{B}_i$ as the metric function to measure the model prediction error, which is given by

$$\delta_{k,i} = h({}^{G_k}\hat{\mathbf{B}}_i, {}^{G_k}\mathbf{B}_i) = \| {}^{G_k}\hat{\mathbf{B}}_i - {}^{G_k}\mathbf{B}_i \|, \tag{21}$$

where ${}^{G_k}\hat{\mathbf{B}}_i$ is the model prediction of ${}^{G_k}\mathbf{B}_i$. ${}^{G_k}\hat{\mathbf{B}}_i$ can be obtained by calibrated parameters $\mathbf{q}_k^{\mathsf{T}} = \{\eta^{\mathsf{T}}, \xi_k^{\mathsf{T}}\}$ and ground truth measurements ${}^{W}\mathbf{B}_i$ according to (15). Lemma 2 shows the variance of $\delta_{k,i}$.

*Lemma 2:* Under Gaussian noise assumption, the variance of $\delta_{k,i}$ is denoted by

$$\sigma_{\delta_{k,i}}^2 = J_{h1}\, {}^{G_k}\hat{\Sigma}_i J_{h1}^{\mathsf{T}} + J_{h2}\, {}^{G_k}\Sigma_i J_{h2}^{\mathsf{T}}, \tag{22}$$

where Jacobian matrices $J_{h1} = \frac{\partial h}{\partial {}^{G_k}\hat{\mathbf{B}}_i}$ and $J_{h2} = \frac{\partial h}{\partial {}^{G_k}\mathbf{B}_i}$.

*Proof:* Since $\delta_{k,i}$ is a function of ${}^{G_k}\hat{\mathbf{B}}_i$ and ${}^{G_k}\mathbf{B}_i$, the uncertainty of $\delta_{k,i}$ comes from their corresponding covariance matrices ${}^{G_k}\Sigma_i$ and ${}^{G_k}\hat{\Sigma}_i$. ${}^{G_k}\Sigma_i$ is given by (14); ${}^{G_k}\hat{\Sigma}_i$ is obtained by the forward propagation of error [30] under first-order approximation

$${}^{G_k}\hat{\Sigma}_i = J_{g1}\, \Sigma_{\mathbf{q}_k} J_{g1}^{\mathsf{T}} + J_{g2}\, {}^{W}\Sigma_i J_{g2}^{\mathsf{T}}, \tag{23}$$

where Jacobian matrices $J_{g1} = \frac{\partial g}{\partial \mathbf{q}_k}$, $J_{g2} = \frac{\partial g}{\partial {}^{W}\mathbf{B}_i}$, and $g$ is the GPR parameterized function. ${}^{W}\Sigma_i$ is obtained from measurement and $\Sigma_{\mathbf{q}_k}$ is the covariance matrix of $\mathbf{q}_k$ which can be extracted by Lemma 1. Since ${}^{G_k}\hat{\mathbf{B}}_i$ and ${}^{G_k}\mathbf{B}_i$ have no correlation, the overall variance of $\delta_{k,i}$ in (22) can be obtained by addition of their uncertainties. ■

$$J_\omega^\mathsf{T}\Sigma_\omega^{-1}J_\omega = \left[\begin{array}{c:c} \mathbf{A} & \mathbf{B} \\ \hdashline \mathbf{C} & \mathbf{D} \end{array}\right] = \left[\begin{array}{ccc:ccc} J_\eta^\mathsf{T}\rho\Sigma J_\eta & J_\eta^\mathsf{T}\rho\Sigma J_{\xi 2} & & \mathbf{0} & \mathbf{0} & J_\eta^\mathsf{T}\rho\Sigma J_{x2} \\ J_{\xi 2}^\mathsf{T}\rho\Sigma J_\eta & J_{\xi 1}^\mathsf{T}\psi\Sigma J_{\xi 1} + J_{\xi 2}^\mathsf{T}\rho\Sigma J_{\xi 2} & & J_{\xi 1}^\mathsf{T}\psi\Sigma J_\pi & J_{\xi 1}^\mathsf{T}\psi\Sigma J_{x1} & J_{\xi 2}^\mathsf{T}\rho\Sigma J_{x2} \\ \hdashline \mathbf{0} & J_\pi^\mathsf{T}\bar{\psi}\Sigma J_{\xi 1} & & J_\pi^\mathsf{T}\bar{\psi}\Sigma J_\pi & J_\pi^\mathsf{T}\bar{\psi}\Sigma J_{x1} & \mathbf{0} \\ \mathbf{0} & J_{x1}^\mathsf{T}\psi\Sigma J_{\xi 1} & & J_{x1}^\mathsf{T}\psi\Sigma J_\pi & {}^C\Sigma + J_{x1}^\mathsf{T}\psi\Sigma J_{x1} & \mathbf{0} \\ J_{x2}^\mathsf{T}\rho\Sigma J_\eta & J_{x2}^\mathsf{T}\rho\Sigma J_{\xi 2} & & \mathbf{0} & \mathbf{0} & {}^G\Sigma + J_{x2}^\mathsf{T}\rho\Sigma J_{x2} \end{array}\right]. \tag{20}$$

## V. Experiments

The proposed method has been validated in physical experiments. We will show the experiment setup and the calibration results with uncertainty analysis in this section.

### A. Experiment Setup

We use GSSI SIR-3000 with 1.6 GHz antennas and the parameters are given as follows: the horizontal sample rate for the wheel encoder is 390 pulses per meter, the two-way travel time of the radar signal is 8 ns, the sample rate for the GPR control unit is 1024 sample/scan, and the dielectric constant in air is 1. To export the GPR images, we use GSSI software RADAN 7. To distinguishing a hyperbola from the background, we apply background subtraction to segment out a foreground hyperbola by subtracting the origin GPR image to the GPR image without a metal ball in the setup. As for camera, we choose an industry grade 10 megapixel CMOS camera (DS-CFMT1000-H) with an external trigger. The intrinsic parameters are calibrated using camera calibration toolbox for Matlab [36]. For the calibration objects, the radius of the metal ball is 19.05 mm and the vertical height $h_i$ is 419.10 mm. The ball checkerboard is with the size of each square 101.0 mm $\times$101.0 mm, and mirror checkerboard is with the size of each square 128.0 mm $\times$128.0 mm.

The calibration data collection follows the procedure mentioned in Section III-B3. We set $n = 24$ and $N = 20$ and we repeat the calibration data collection procedure to collect two datasets: one for calibration and one for testing.

### B. Calibration Results

We use the calibration dataset to estimate the relative pose between the camera and the GPR. The calibration results are shown as follows: ${}^G_C\mathbf{t} = [-10.2, -108.3, 1246.0]^\mathsf{T}$ mm and $[\theta_x, \theta_y, \theta_z]^\mathsf{T} = [-1.9945, 0.0211, 0.0199]^\mathsf{T}$ rad, where $(\theta_x, \theta_y, \theta_z)$ is the Euler angle representation of ${}^G_C\mathbf{R}$.

### C. Direct Approach vs. Dual Modal Calibration Optimization

We compare the calibration results from a direct approach with the results from our approach in this paper. The former is to compute the results by combining [21] with mirror-based camera calibration directly. The latter estimates not only the relative pose but also the calibration setting, which consists of camera and mirror positions. To evaluate two approaches, we first use $D_i$ and $h_i$ in testing set to estimate ${}^{G_k}\mathbf{B}_i$ and then map it into world frame as ${}^W\hat{\mathbf{B}}_i$. Then we use the Euclidean distance between the estimator ${}^W\hat{\mathbf{B}}_i$ and the measurement ${}^W\mathbf{B}_i$ for error analysis, where ${}^W\mathbf{B}_i$ is served as ground truth. The results show that the mean error and standard deviation (SD) are 18.68 mm and 5.48 mm for the direct approach, while our mean error and SD are 6.67 mm and 3.40 mm. As a result, our approach in this paper achieves higher accuracy than the direct approach. Besides, considering the fact that the GPR signal wave length is 18.75 cm, the results are satisfying.

### D. Model Prediction Errors and Uncertainty Analysis

In this section, we evaluate if our uncertainty analysis in Section IV-D can capture the prediction error of the calibrated model. Since we do not have the ground truth to validate our calibration results, we use $D_i$ and $h_i$ in testing set to estimate ${}^{G_k}\mathbf{B}_i$, which is served as ground truth. And we estimate ${}^{G_k}\hat{\mathbf{B}}_i$ by transforming ${}^W\mathbf{B}_i$ through ${}^{C_k}_W\mathbf{T}$ and ${}^G_C\mathbf{T}$. We also evaluate the calibration result by computing the Euclidean distance between ${}^{G_k}\mathbf{B}_i$ and ${}^{G_k}\hat{\mathbf{B}}_i$. To obtain the average error for each metal ball center position, we compute the model prediction for each $\{G_k\}$ according to Lemma 2 and take the average of them by using $\delta_i = \frac{\sum_{k=1}^N \delta_{k,i}}{N}$. Hence the expected value and variance of $\delta_i$ can be estimated by sample mean and sample variance. We have the error and the predicted $\sigma_{\delta_i}$ for the 24 testing samples listed in Table I. More specifically, the measurement errors for metal ball center position measurements have a variance of 8 mm$^2$ in each dimension. This may be caused by radar accuracy and structural deformation under weight. Hence, ${}^W\Sigma_i = 8\mathbf{I_3}$ and $\sigma_{h_i}^2 = 8$ for $h_i$. Besides, the variance for points on GPR and camera images are set to 1. The results agree with our analysis as 66.67% errors fall in the 1-$\sigma$ range of the calibrated model prediction.

TABLE I
The predicted SD of $\delta_i$ vs its actual value

| $i$ | $\sigma_{\delta_i}$(mm) | $\delta_i$(mm) | $i$ | $\sigma_{\delta_i}$(mm) | $\delta_i$(mm) |
|---|---|---|---|---|---|
| 1 | 6.17 | 3.67 | 13 | 17.33 | 4.41 |
| 2 | 7.56 | 3.44 | 14 | 28.45 | 4.15 |
| 3 | 6.43 | 7.24 | 15 | 8.52 | 2.23 |
| 4 | 6.69 | 5.88 | 16 | 10.94 | 6.42 |
| 5 | 14.08 | 3.26 | 17 | 6.53 | 5.65 |
| 6 | 5.79 | 3.14 | 18 | 7.61 | 3.45 |
| 7 | 8.36 | 8.24 | 19 | 7.30 | 5.06 |
| 8 | 9.29 | 9.19 | 20 | 5.66 | 10.33 |
| 9 | 13.61 | 14.03 | 21 | 6.90 | 8.82 |
| 10 | 38.13 | 2.08 | 22 | 6.08 | 13.27 |
| 11 | 5.52 | 8.92 | 23 | 22.59 | 7.69 |
| 12 | 6.02 | 8.08 | 24 | 5.83 | 11.46 |

## VI. Conclusions and Future Work

We proposed a calibration system for the relative pose calibration of a GPR and a camera. We designed an artificial planar bridge with a planar mirror as the calibration platform. We modeled the camera projection with mirror reflection transformation and GPR imaging process. By using ball checkerboard and metal ball as calibration object, we estimated camera and mirror poses from camera images and extracted

hyperbolas in the GPR image to recover metal ball coordinates in the GPR frame. The MLE was employed to estimate the rigid body transformation between the two sensors. We provided the closed form error analysis for our calibration models. The physical experiments confirmed our results.

In the future, we will collect data on real bridges and fuse the data from different sensors for automatic in-traffic bridge inspection.

## ACKNOWLEDGMENT

We would like to thank Paul Carlson from Texas A&M Transportation Institute (TTI) for insightful inputs. We also thank prof. Jingang Yi from Rutgers University for valuable inputs. We would also like to thank H. Cheng, B. Li, J. Chen, M. Jin, Y. Sun, A. Kingery, Y. Yu, H. Wang, and H. Li for their input and contributions to the NetBot Lab at Texas A&M University.

## REFERENCES

[1] A. Elatta, L. P. Gen, F. L. Zhi, Y. Daoyuan, and L. Fei, "An overview of robot calibration," *Information Technology Journal*, vol. 3, no. 1, pp. 74–78, January 2004.

[2] S. Ross, *Introduction to Probability Models, Ninth Edition*. Academic Press, 2007.

[3] B. Siciliano and O. Khatib, *Springer Handbook of Robotics*. Springer Science & Business Media, 2008.

[4] D. Song, N. Qin, and K. Goldberg, "A minimum variance calibration algorithm for pan-tilt robotic cameras in natural environments," in *IEEE International Conference on Robotics and Automation (ICRA), Orlando, Florida*, May 2006.

[5] K. H. Strobl and G. Hirzinger, "Optimal hand-eye calibration," in *IEEE/RSJ International Conference on Intelligent Robots (IROS), Beijing, China*, 2006, pp. 4647–4653.

[6] J. Fraden, *Handbook of Modern Sensors: Physics, Designs, and Applications*. Springer Science & Business Media, 2004.

[7] Z. Zhang, "A flexible new technique for camera calibration," *IEEE Transactions on Pattern Analysis and Machine Intelligence*, vol. 22, no. 11, pp. 1330–1334, 2000.

[8] J. Heikkila and O. Silven, "A four-step camera calibration procedure with implicit image correction," in *IEEE Computer Society Conference on Computer Vision and Pattern Recognition (CVPR'97)*, 1997, pp. 1106–1112.

[9] D. Song, C. Kim, and J. Yi, "Simultaneous localization of multiple unknown and transient radio sources using a mobile robot," *IEEE Transactions on Robotics*, vol. 28, no. 3, pp. 668–680, June 2012.

[10] C. Gao and J. R. Spletzer, "On-line calibration of multiple lidars on a mobile vehicle platform," in *IEEE International Conference on obotics and Automation (ICRA), Anchorage, AK*, 2010, pp. 279–284.

[11] N. Muhammad and S. Lacroix, "Calibration of a rotating multi-beam lidar," in *IEEE/RSJ International Conference on Intelligent Robots (IROS), Taipei*, 2010, pp. 5648–5653.

[12] Q. Zhang and R. Pless, "Extrinsic calibration of a camera and laser range finder (improves camera calibration)," in *IEEE/RSJ International Conference on Intelligent Robots (IROS), Sendai, Japan*, vol. 3, 2004, pp. 2301–2306.

[13] F. Vasconcelos, J. P. Barreto, and U. Nunes, "A minimal solution for the extrinsic calibration of a camera and a laser-rangefinder," *IEEE transactions on pattern analysis and machine intelligence*, vol. 34, no. 11, pp. 2097–2107, 2012.

[14] L. Zhou, "A new minimal solution for the extrinsic calibration of a 2d lidar and a camera using three plane-line correspondences," *IEEE Sensors Journal*, vol. 14, no. 2, pp. 442–454, 2014.

[15] D. J. Daniels, *Ground Penetrating Radar, 2nd Edition*. The Institution of Engineering and Technology, 2004, vol. 1.

[16] H. M. Jol, *Ground Penetrating Radar Theory and Applications*. Elsevier, 2008.

[17] A. Annan, *Electromagnetic Principles of Ground Penetrating Radar*. Elsevier, 2009, vol. 1.

[18] T. Evans, R. Ponticelli, E. Garcia, P. Gonzalez de Santos, and M. Armada, "A scanning robotic system for humanitarian de-mining activities," *Industrial Robot: An International Journal*, vol. 35, no. 2, pp. 133–142, 2008.

[19] H. M. La, N. Gucunski, S.-H. Kee, J. Yi, T. Senlet, and L. Nguyen, "Autonomous robotic system for bridge deck data collection and analysis," in *IEEE/RSJ International Conference on Intelligent Robots (IROS), Chicago, IL*, 2014, pp. 1950–1955.

[20] P. Furgale, T. D. Barfoot, N. Ghafoor, K. Williams, and G. Osinski, "Field testing of an integrated surface/subsurface modeling technique for planetary exploration," *The International Journal of Robotics Research*, vol. 29, no. 12, pp. 1529–1549, October 2010.

[21] C. Chou, S. Yeh, J. Yi, and D. Song, "Extrinsic calibration of a ground penetrating radar," in *IEEE International Conference on Automation Science and Engineering (CASE), Fort Worth, Texas*, Aug. 2016.

[22] R. K. Kumar, A. Ilie, J.-M. Frahm, and M. Pollefeys, "Simple calibration of non-overlapping cameras with a mirror," in *IEEE Computer Society Conference on Computer Vision and Pattern Recognition (CVPR)*, 2008, pp. 1–7.

[23] J. A. Hesch, A. I. Mourikis, and S. I. Roumeliotis, "Determining the camera to robot-body transformation from planar mirror reflections," in *IEEE/RSJ International Conference on Intelligent Robots (IROS), Nice, France*, 2010, pp. 3865–3871.

[24] P. Lébraly, C. Deymier, O. Ait-Aider, E. Royer, and M. Dhome, "Flexible extrinsic calibration of non-overlapping cameras using a planar mirror: Application to vision-based robotics," in *IEEE/RSJ International Conference on Intelligent Robots (IROS), Taipei*, 2010, pp. 5640–5647.

[25] R. Rodrigues, J. P. Barreto, and U. Nunes, "Camera pose estimation using images of planar mirror reflections," in *European Conference on Computer Vision (EVVC)*. Springer, 2010, pp. 382–395.

[26] A. Agha-mohammadi and D. Song, "Robust recognition of planar mirrored walls using a single view," in *IEEE International Conference on Robotics and Automation (ICRA), Shanghai, China*, May 2011.

[27] K. Takahashi, S. Nobuhara, and T. Matsuyama, "A new mirror-based extrinsic camera calibration using an orthogonality constraint," in *IEEE Computer Society Conference on Computer Vision and Pattern Recognition (CVPR)*, 2012, pp. 1051–1058.

[28] Y. Lu, D. Song, H. Li, and J. Liu, "Automatic recognition of spurious surface in building exterior survey," in *IEEE International Conference on Automation Science and Engineering (CASE), Madison, Wisconsin*, Aug. 2013.

[29] G. Long, L. Kneip, X. Li, X. Zhang, and Q. Yu, "Simplified mirror-based camera pose computation via rotation averaging," in *IEEE Computer Society Conference on Computer Vision and Pattern Recognition (CVPR)*, 2015, pp. 1247–1255.

[30] R. Hartley and A. Zisserman, *Multiple View Geometry in Computer Vision, 2nd Edition*. Cambridge University Press, 2004.

[31] V. Lepetit, F. Moreno-Noguer, and P. Fua, "Epnp: An accurate o(n) solution to the pnp problem," *International Journal of Computer Vision*, vol. 81, no. 2, pp. 155–166, 2008.

[32] S. Li, C. Xu, and M. Xie, "A robust o(n) solution to the perspective-n-point problem," *IEEE Transactions on Pattern Analysis and Machine Intelligence*, vol. 34, no. 7, pp. 1444–1450, July 2012.

[33] R. Hartley, J. Trumpf, Y. Dai, and H. Li, "Rotation averaging," *International Journal of Computer Vision*, vol. 103, no. 3, pp. 267–305, 2013.

[34] C. Warren and A. Giannopoulos, "Investigation of the directivity of a commercial ground-penetrating radar antenna using a finite-difference time-domain antenna model," in *14th International Conference on Ground Penetrating Radar (GPR)*, 2012, pp. 226–231.

[35] B. Horn, "Closed form solution of absolute orientation using unit quaternions," *Journal of the Optical Society A*, vol. 4, no. 4, pp. 629–42, 1987.

[36] J.-Y. Bouguet, "Camera calibration toolbox for matlab," 2004.